Nonlinear finite-difference time-domain method for exciton-polaritons: application to saltatory conduction in polariton neurons

K. Dini,[1] H. Sigurðsson,[2,3] N. W. E. Seet,[1] P. M. Walker,[4] and T. C. H. Liew[1]

[1]*Division of Physics and Applied Physics, School of Physical and Mathematical Sciences, Nanyang Technological University 637371, Singapore*
[2]*Institute of Experimental Physics, Faculty of Physics, University of Warsaw, ul. Pasteura 5, PL-02-093 Warsaw, Poland*
[3]*Science Institute, University of Iceland, Dunhagi 3, IS-107 Reykjavik, Iceland*
[4]*School of Mathematical and Physical Sciences, University of Sheffield, S3 7RH, Sheffield, UK*
(*timothyliew@ntu.edu.sg)
(*kevin.dini74@gmail.com)
(Dated: December 5, 2024)

Recently emerging complex photonic structures exhibiting giant optical nonlinearity through strong light-matter coupling require new theoretical approaches to accurately capture the interplay of the photonic and interacting-matter degrees of freedom. Extending the finite-difference time-domain method, we develop an algorithm for solving the nonlinear Maxwell-Bloch equations. This allows first-principles modeling of exciton-polariton systems for arbitrarily complex photonic structures with photon-exciton coupling and frequency dependent nonlinear response included without approximations or phenomenological parameters. We first validate the algorithm by reproducing the bistable hysteresis cycle of polaritons in the nonlinear regime. We then give a key example of its utility by simulating polariton dynamics in integrated photonic circuitry composed of spatially localised bistable nodes connected by high speed waveguides. We propose a polariton circuit element inspired by saltatory conduction in biological neurons. This design supports faster polariton signal propagation than previous designs, however, requires a full account of the nonlinear field distributions in both propagation and growth directions to be calculated.

The spatial and temporal dynamics of exciton-polaritons in semiconductor microcavities is typically described by a generalized two-dimensional (2D) nonlinear Schrödinger equation, or Gross-Pitaevskii equation when concerning polariton Bose-Einstein condensates [1]. This treatment has been largely successful in describing a wide variety of experimentally observed effects, for example: vortices [2], solitons [3], four-wave mixing [4], and various spin patterns [5, 6].

With advances in growth technology, many groups have developed and studied spatially patterned microcavities, where the planar geometry is patterned into arbitrary shapes, including channels [7, 8], pillars [9], waveguides [10–14], gratings [15–17], and lattices [18, 19]. The theoretical description of these systems is typically made in an ad-hoc fashion, where a spatially varying 2D potential is chosen phenomenologically to match the considered geometries. As the potential is not derived from first principles, its parameters, such as its depth, are only understood as fitting parameters. Furthermore, the effects of confinement on the polarization structure, such as polarization splitting in channels [20], pillars [21], or optical traps [22] with reduced axial symmetry can also only be described phenomenologically within the nonlinear Schrödinger framework. When considering the coupling between different parts of a structured microcavity, the possible mediation by modes propagating in the plane of the structure (such as guided modes) is inaccessible in the usual 2D Schrödinger model. These effects are better treated by solving Maxwell's equations, for which commercial software is often used. However, as such software is not designed specifically for exciton-polariton systems, it does not directly model exciton-photon coupling and, crucially, it offers no treatment of the effective optical non-linearity stemming from exciton-exciton interactions [23, 24]. This exhibits complex saturating and highly frequency dependent behaviour. Apart from narrowband simulations with perturbatively weak interactions, the exciton-polariton non-linear behaviour cannot be modelled by the simple third order photon non-linear response available in commercial packages (see Appendix A). Here, we develop the Maxwell-Bloch equations and demonstrate their solution using a finite-difference time-domain (FDTD) algorithm. We show that this allows the reproduction of nonlinear effects, such as polariton bistability [25], where nonlinearity is included in the equation for the polarization field.

Using our algorithm, we address a critical problem in the field of integrated polaritonics concerning the design of efficient logic gates, diodes, and transistors [26–32] that are coupled together via the ballistic propagation of polaritons [33–36]. The problem is that planar microcavity polaritons have a small in-plane wavevector component with typical group velocity of only 1% the speed of light [6]. Since polaritons decay at a nearly constant GHz rate their slow in-plane propagation results in considerable signal attenuation. A potential solution, which has attracted significant attention, is to use waveguided polaritons that travel around 20% of the speed of light (in vacuum) [10–14]. The trouble, however, is that fast moving polaritons spend little time in one area and so their nonlinear effects are diminished; waveguided polaritons have not shown, for example, bistability. Here, we propose a microcavity structure, inspired by the behavior of real biological neurons, wherein cavity nodes (i.e., neuron nodes) contain localized nonlinear polaritons but are coupled together by waveguiding channels supporting fast propagating polaritons. We show that binary information encoded in the local bistable state of the nodes can be transported between nodes at least

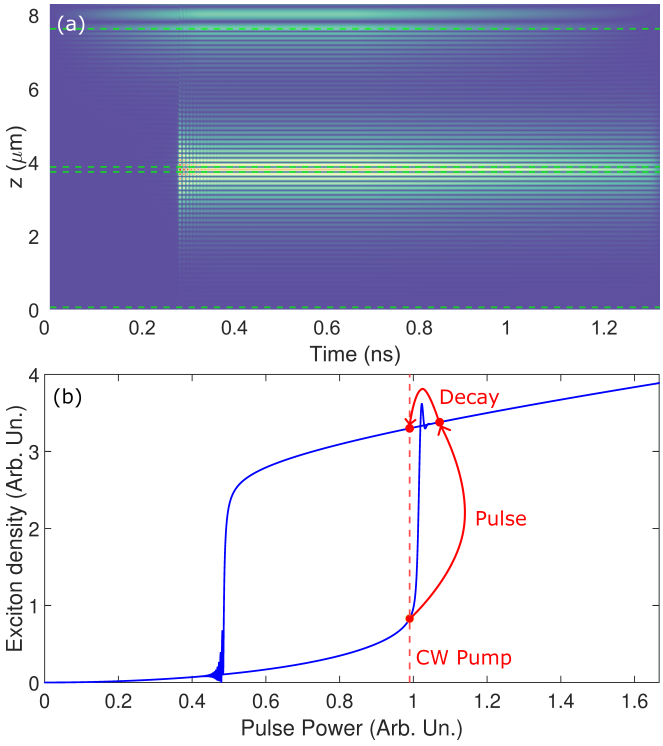

Figure 1: (a) Time dependence of the intensity of the electric field in the 1D microcavity structure. The dashed green lines correspond to the edges of the Bragg mirrors and the cavity. The coherent pump is linearly ramped up in power then down on a 1.3 ns interval (i.e., a 1.3ns long triangular pulse). (b) Density of excitons measured at the position of the active material (blue curve). The principle of the bistable switch is also displayed: the CW pump (dashed line) sets the system in the lower bistable state, close to the bistability threshold. A pulse is then injected to switch the system into the upper bistable branch. Decay after the pulse brings the system to the upper bistable state at the power of the CW pump.

ten times faster than in previous proposals. Our system can be regarded as a polaritonic analog of neuronal saltatory conduction [37] complementing the recent surging development in neuromorphic cavity polaritonics [38–46]. To model the coupling between the localized nonlinear modes and waveguided modes, we rely on the aforementioned nonlinear FDTD algorithm, noting that previous theoretical frameworks are insufficient for accurate prediction of the total (nonlinear) signal transfer speed (a key figure of merit) in the considered geometry.

This article is organized as follows: we first review the basic linear FDTD method used to time-evolve Maxwell equations; we then expand this formalism to include the exciton resonance and the exciton-exciton interaction using coupled Bloch equations; finally, we apply this new formalism to study the aforementioned polariton saltatory conduction.

I. NONLINEAR FDTD METHOD

The basic FDTD algorithm is used to evolve Maxwell's equations, represented on a computational grid, with finite steps in time. The technique is commonly used to describe the behaviour of electromagnetic waves in the vicinity of structures with arbitrary spatial geometry [47–50]. We will first review this basic formalism for the treatment of purely photonic problems. Then, we will show how to introduce excitons that affect the local polarization through the Bloch equations. This offers an accurate description of both exciton-photon coupling and nonlinearity in arbitrary spatial geometries. We begin by writing Maxwell's equations for a non-magnetic system:

$$\nabla \times \mathbf{H} = \frac{\partial \mathbf{D}}{\partial t} + \mathbf{J_b} + \sigma_e \mathbf{E} \tag{1}$$

$$\nabla \times \mathbf{E} = -\frac{\partial \mathbf{B}}{\partial t} - \sigma_m \mathbf{H} \tag{2}$$

$$\nabla \cdot \mathbf{D} = 0 \tag{3}$$

$$\nabla \cdot \mathbf{H} = 0; \tag{4}$$

$\mathbf{E}$ is the electric field; $\mathbf{D}$ is the electric displacement vector; $\mathbf{H}$ is the magnetic field strength vector; $\mathbf{B}$ is the magnetic flux density vector; $\mathbf{J_b}$ is the bound electric current density, where for simplicity we only consider bound charges induced by the active layer and σ_e and σ_m are the electric and magnetic conductivities, respectively. Consequently, the density of free charges is set to be null. We can also write the following constitutive relations: $\mathbf{D} = \varepsilon \mathbf{E}$ and $\mathbf{B} = \mu_0 \mathbf{H}$, where μ_0 is the vacuum permeability and ε is the permittivity of the material. This leads to Maxwell curl equations for $\mathbf{H}$ and $\mathbf{E}$:

$$\begin{aligned} \nabla \times \mathbf{H} &= \varepsilon \frac{\partial \mathbf{E}}{\partial t} + \sigma_e \mathbf{E} + \mathbf{J_b} \\ \nabla \times \mathbf{E} &= -\mu_0 \frac{\partial \mathbf{H}}{\partial t} - \sigma_m \mathbf{H} \end{aligned} \tag{5}$$

The FDTD algorithm consists of solving the set of Maxwell's equations using the Yee algorithm that updates the magnetic and electric fields at every point in space at every time step of a time marching iteration. Both electric and magnetic fields, and the auxiliary fields are sampled at discrete positions and times. Since both fields are interdependent, they are not updated simultaneously or measured at the same position. Rather, the magnetic field is updated at times $(n+1/2)\Delta t$ and the electric field at times $n\Delta t$, where n is a positive integer and Δt is the time-sampling period. Moreover the sampling points of the fields are chosen following a specific grid, the so-called Yee grid [51] allowing to treat the magnetic and electric fields separately. We here choose to work with a Cartesian grid but it should be noted that other coordinate systems could be used to fit the symmetries of a specific system [48].

Applying the FDTD method on the set of Maxwell equations (5), we replace the derivatives by summations of components of the fields on the Yee grid, and use a set of update equations for all components of the electric and magnetic fields (see Appendix B). However, Maxwell equations only

describe the dynamics of the electromagnetic field in the system. The exciton population, exciton-exciton interaction and their coupling to light is not yet described by this formalism. In order to extend this formalism and include the excitons, we need to express its dynamics using an auxiliary field that can be inserted in the Maxwell equations [52]. Studying the dynamics of charged carriers considering Coulomb effects, it can be shown that the effects of excitons on the system can be described using the interband polarization vector [53] with dynamics ruled by the semiconductor Bloch equations. These equations describe the dynamics of the polarization vector along with the dynamics of the population of charged carriers.

Since interactions between excitons are central in polariton physics, it is necessary to incorporate them in the dynamics of the polarization field. This description cannot be done using the Bloch equations on the electron-hole basis, but needs to be done on the exciton one. After formulating the electron-hole second quantization Hamiltonian including Coulomb effects and the interaction with external electric field, one can perform the so-called Usui transform, and switch from the fermionic operators to bosonic ones. We consider the same approximations under which Eqs.(26) and (27) of Ref [54] were derived and re-express the polarization $\mathbf{P}(\mathbf{r},t)$ and exciton population $N(\mathbf{r},t)$ Bloch equations as:

$$i\frac{\partial \mathbf{P}}{\partial t} = (\omega_0 - i\gamma)\,\mathbf{P} - \Omega\mathbf{E} + \alpha N\mathbf{P} \tag{6}$$

$$\frac{\partial N}{\partial t} = -2\,\mathrm{Im}\,(\Omega\mathbf{E}\cdot\mathbf{P}^*) \tag{7}$$

where γ is the homogeneous broadening, $\hbar\omega_0$ is the exciton transition energy, Ω is the oscillator strength and α is the exchange interaction coefficient.

In order to include the polarization vector in the Maxwell equations (5), we relate it to the bound charge current through:

$$\mathbf{J_b} = \frac{\partial \mathbf{P}}{\partial t}. \tag{8}$$

Then using the FDTD method we obtain the update equation for the excitons (see Appendix B for more details). From here on we refer to our algorithm as the nonlinear FDTD (NL-FDTD).

It should be noted that we have assumed point-like interactions between excitons in our theory, corresponding to the most common form of interactions in popular inorganic-based microcavities. We note that some samples have been engineered to show longer range interactions, such as dipolar polariton interactions [57] in waveguides, which achieve impressive interaction strength and propagation speed. It would be interesting to find if this scheme could also exhibit local bistability, which we consider an important foundation for the representation of binary signals.

In the same way as commonly used mean-field theories of exciton-polariton dynamics are based on a single interaction strength parameter, our developed theory also assumes such a parameter as an input. The polariton-polariton interaction strength has been measured with different techniques

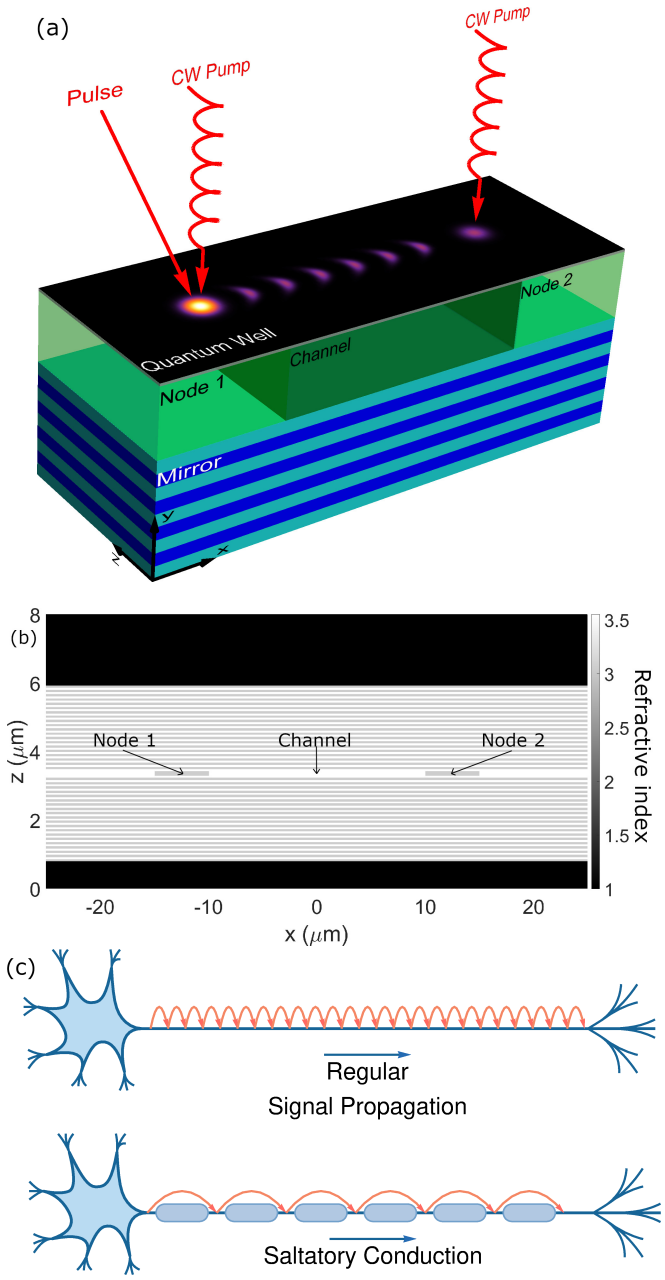

Figure 2: (a) Sketch of the system. Blue - Bragg Mirrors, Light green - Nodes ($Ga_{0.05}Al_{0.95}As$ $n_1 = 3.05$), Dark green - Channels ($Ga_{0.80}Al_{0.20}As$ $n_2 = 3.55$). For clarity, the upper half of the system is not shown. (b) Corresponding refractive index distribution. (c) Neurons schematic displaying the differences between regular signal propagation and saltatory conduction.

and there is a significant spread in the reported values [58]. In practice, even though this parameter may not be known accurately, the commonly used mean-field theory has been able to describe experiments by taking either the polariton intensity or interaction strength (or both) as fitting parameters. The purpose of our present work is to describe how one can model patterned microcavity structures, albeit with no more knowl-

edge of the interaction strength as in planar structures.

In using the Maxwell equations, we have assumed a coherent field and neglected energy relaxation mechanisms such as the scattering with phonons. Indeed, while dissipative losses due to phonon coupling are to some extent included in the exciton homogeneous linewidth, it is difficult to include the inhomogeneous ensemble of excitons. These are the same assumptions used in the common application of mean-field theories to planar samples and so should be equally applicable to the spatially patterned microcavities that we address here. Nevertheless, we note that in some materials, especially those intended for room temperature operation, such as organics and perovskite, phonon-induced effects including dispersion renormalization may be dominant [59]. In principle, they could be accounted by coupling the electric and polarization fields to a phonon potential [60].

II. NUMERICAL SIMULATIONS

A. Optical bistability

Now that we have defined the iterative expressions for both Maxwell and Bloch equations including light-matter coupling and exciton-exciton interactions, we can study a simple system to check the validity of our approach. A very well studied nonlinear effect in polariton physics is bistability. Under a near-resonant optical excitation, exciton-exciton interactions manifest as a non-linear dependency between the polariton population and pump power, displaying a hysteresis response [25]. Polariton bistability of this form is a precursor to fundamental effects such as spinor multistability [61, 62], compactons [63], spatial patterns [64], bistable topological states [65], and long-lived vortex streets [66]. Bistability also serves for encoding information for polariton memories [27], switches [67, 68], circuits [69], Ising spins [70] and cellular automata [71].

In order to verify this phenomenon using our algorithm, we consider a one-dimensional (i.e., only z-axis) GaAlAs based λ microcavity with an embedded GaAs quantum well. The mirrors on each side consist of 10 pairs of $Ga_{0.05}Al_{0.95}As$ and $Ga_{0.8}Al_{0.2}As$ with respective refractive index of $n_1 = 3.05$ and $n_2 = 3.55$ and thickness $L_1 = 67.2$ nm and $L_2 = 57.7$ nm which match the Bragg condition. While the low number of layers leads to a broad cavity linewidth it avoids excessive numerical run-time while not changing the observed effects. The quantum well consists of a 10 nm thick layer of GaAs with refractive index $n = 3.62$. The light matter coupling constant Ω is set such that the Rabi splitting is 20 meV. Without loss of generality we set the interaction constant $\alpha = 1\mu eV.\mu m^{-1}$. The exciton is considered to have a typical nonradiative lifetime of 500 ps. We use a TE polarized coherent electromagnetic source with an energy blue-detuned 2Γ from the bottom of the Lower Polariton Branch (LPB), where Γ^{-1} is the polariton lifetime. The intensity is linearly ramped up from 0 to a maximum value above the bistable threshold and then linearly ramped down (i.e., triangular pulse). We show in Fig. 1 the polariton (exciton) density versus pump power displaying the prototypical optical hysteresis cycle in full accordance with analytical predictions [56]. Indeed, since the pump is slightly detuned from the LPB at low powers, the injection of polaritons is suboptimum but as the intensity increases, the LPB blue-shifts and gets slowly closer to resonance resulting in the non-linear dependence of the population versus power. For some value of the laser power (threshold power), the lower branch gets close to resonance with the laser, making the injection close to optimum and leading to a jump in the population. This effect along with the hysteretic behaviour are both characteristic to polaritons in the bistable regime and are observed using our NL-FDTD alrorithm.

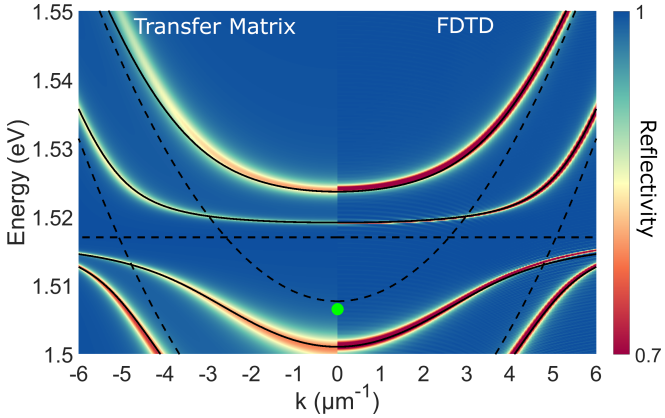

Figure 3: Reflectivity spectrum of the saltatory structure calculated with Transfer Matrix method (left) and FDTD (right). In the case of the TMM, the spectrum is successively calculated for a 'node' cavity and for a 'channel' one. The spectra are then superimposed. For the FDTD calculation, we successively calculate the spectrum for different positions of the source along the x-axis and take the average of the results. The green dot shows the energy of the pump used to obtain the bistable state.

For completeness, we also calculated the dispersion relation of a microcavity used in the existing literature [72] and found excellent agreement between the calculated and previously published experimental polariton dispersion (see Appendix C). This establishes that our algorithm is suitable for the modelling of real-world structures.

B. Waveguided Coupled nodes

We next address the issue of short range polariton propagation due to photonic losses. A theoretical solution was proposed in the form of polariton neurons [73, 74] where a continuous pump applied to the microcavity places spatially separated components in a locally bistable regime. Binary information, stored in the local bistable state was found to propagate along channels, which could have arbitrary shape. The propagation length was determined by the extent of the applied laser field, rather than having any limitation due to the short polariton lifetime. This is because information is propagated as a successive switching of the locally bistable state

rather than pure ballistic propagation of polaritons, in analogy to how the successive switching of local potentials in biological neurons carries a signal much longer than that expected from diffusion of ions along the neurons length. However, even though losses are compensated, and the polariton neuron scheme was shown to be universally complete [69], the estimated signal propagation speed remains around 1% the speed of light. To increase their signal transport speed, vertebrate neurons evolved to use a layer of fat-containing cells (the Myelin Sheath) to separate the neuron into insulating segments that connect a series of nodes formed by gaps in the cells (see Figure 2c). The signal in this structure jumps between nodes, in a process known as saltatory conduction, travelling over ten times faster than the signal in the neurons of invertebrates. Extending the analogy with biological neurons for polariton signal propagation, we consider here a polariton channel periodically modulated with low refractive index sections that form nodes, connected by higher refractive index sections. The nodes are operated in a regime of local bistability, such that they support and maintain clearly defined binary signal amplitudes. The higher refractive index sections support waveguided signals. In these segments polaritons travel at around 15% of the speed of light [13, 75, 76] and can trigger a fast jump of the signal within the nodes, restoring lost amplitude. The velocity in the channel depends on the difference between the refractive indices of the node and the channel.

We consider a GaAlAs modulated cavity where the refractive index varies spatially along the x-axis (see Fig. 2). The *nodes* where the signal will be re-amplified corresponds to the low refractive index area, whereas the *channel* where the signal propagates at high velocity corresponds to a high refractive index area. We first calculate the reflectivity spectrum of the structure using the linear FDTD algorithm and compare it with the transfer matrix method (TMM) reflectivity spectra. Figure 3 compares the dispersion obtained by the two methods. The excellent agreement confirms that the algorithm functions properly and that the parameters are chosen properly (see Fig. 3). Such a structure could in principle be made using an etch and overgrowth method [77].

A near-resonant quasi-CW (with constant power for the duration of the simulation) optical pump, with Gaussian spatial profile, excites polaritons at each node at normal incidence (see Figure 2) for the duration of the simulation. A small pump detuning Δ_P, with respect to the LPB is chosen such that the polaritons exhibit bistability at each node (see green dot in Figure 3). The intensity of the pump is adjusted such that node polaritons are initially in the lower bistable branch but can be triggered with a strong enough signal to the upper branch. To simulate the dynamics of this system we use the aforementioned 2D NL-FDTD.

For the first 15ps (see Fig. 4), we first slowly linearly increase the quasi-CW pumps up to a power slightly below the bistable threshold, here "slow" means much longer than the characteristic timescales of the saltatory polariton. We then keep the pump intensity constant for another 17ps in order to reach a stationary regime. We then add a weak Gaussian pulse at $t = 32$ ps on the left node. We observe that the left node completes its switch to the upper bistable state within a few ps. It should be noted that the speed of the bistable switching depends strongly on how close to threshold the quasi-CW pump is. We here had to set the pump relatively far from threshold compared to what is possible in order to keep the ramp time short. If the considered ramp time is too short, the system may enter the upper state before reaching the stationary regime as some intensity oscillations are observed when the quasi-CW pump becomes constant.

After the pulse is injected, a corresponding polaritonic signal from the left node travels through the channel, at around 5% the speed of light, to reach the second node after 2 ps. The right node then switches to the upper state. Because of the channel shortness, the delay between the pulse and the right node activation is dominated by the time it took the nodes to activate after receiving the signal, as opposed to the polariton travel time within the channel. The intensity of the electric field is measured at the position of the quantum well.

The speed of the signal is related to the ratio of the refractive indices in the node and the channel. This ratio also controls the intensity of the signal transferred from the node to the channel. Therefore increasing the speed decreases the intensity transferred in the channel, as discussed further in see Appendix D. This trade-off opens a way for improvement of this structure by lowering the minimum intensity in the channel to switch the second node through making the quasi-CW closer to the bistable threshold and adjusting the refractive index of the channel to increase the signal velocity. These optimizations cannot be performed using previously developed theoretical and numerical tools, as the described figures of merit depend strongly on the three-dimensional spatial structure of the polaritonic modes in the different regions, and their overlap, all of which are affected by the time-varying non-linear potential. This shows the benefits and advantages of our method, which can fully account for the interplay between complex photonic structure and giant non-linear response of polariton systems, taking real device parameters as inputs.

III. DISCUSSION AND CONCLUSIONS

We have developed a new method to describe exciton polaritons in complex structures from first principles by solving the coupled Maxwell-Bloch equations using the FDTD algorithm. Already existing algorithms, such as linear response theory FDTD to treat the exciton resonance or photonic FDTD including the Kerr non-linearity, are not adapted to describe accurately polariton systems. While the first one describes the exciton polariton in the linear regime only, the second one describes the non-linearity based on a different fundamental effect leading to an incorrect description of the polariton system in the general case. A key feature of polaritons, which affects just about any figure of merit in polariton devices is the blueshift. Introducing the polariton non-linearity as a Kerr-type leads to a blueshift of the photonic mode whereas introducing it using exciton-exciton interaction – as in our model – leads to the correct blueshift of the exciton resonance (see Appendix A).

In order to study the transport of a signal from one bistable

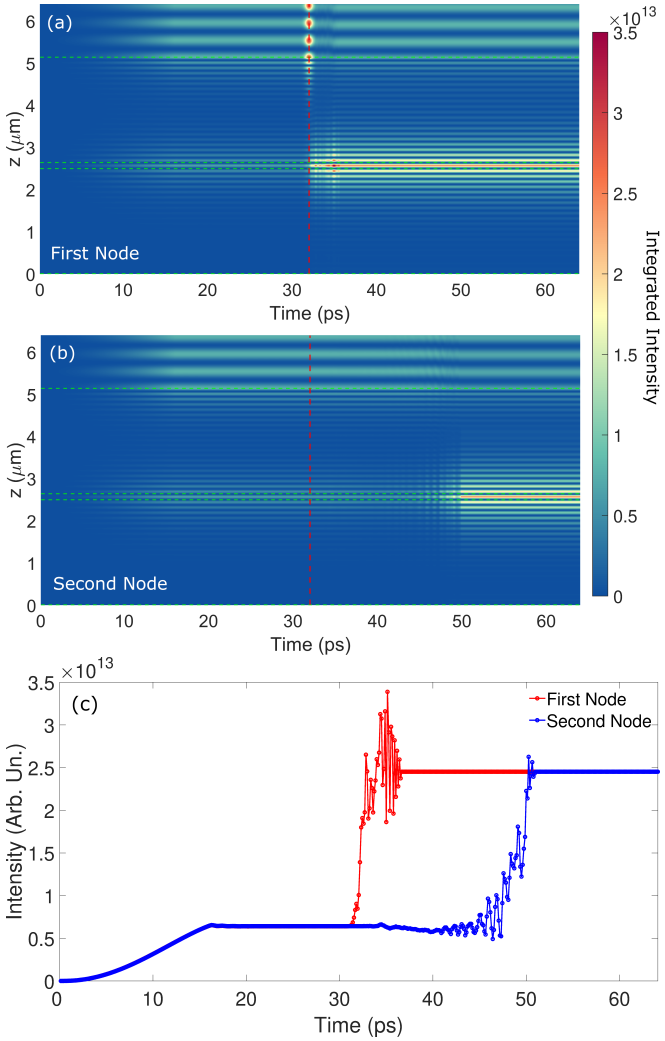

Figure 4: Integrated intensity of the electric field at the first (a) and second (b) nodes, arbitrary unit. The pump at two nodes is ramped up to reach just below the bistable threshold at 15 ps. A small pulse is then sent on the left node at 32 ps, the left node switches followed by the right one after about 20ps. (c) Integrated intensity at the first (red) and second (blue) nodes measured at the position of the active layer. The optical signal is received by the second nodes a few ps after the pulse, the bistable switch takes a dozen ps longer.

state to another via a waveguided mode on large distances and at large speeds, it is critical to calculate accurately different figures of merit such as the signal propagation speed, switching time, and signal decay rate. To calculate the switching speed for instance, one needs to determine the coupling strength between the locally bistable modes and the waveguided modes, which depends on how the modes interact in the three-dimensional structure. Gross-Pitaevskii equations could describe the same process based on an ad-hoc phenomenologically introduced coupling constant between two sets of modes (low k and high k). However, as the coupling speed will depend on this a priori unknown constant, the Gross-Pitaevskii equation itself can not *predict* the coupling speed at all. Furthermore, our treatment allows that the coupling may actually not be constant but affected itself by non-linearity, which will influence the three-dimensional structure of the modes.

Therefore, while existing methods can describe polariton systems with strong limitations, our model allows for a correct and accurate description of the polaritons dynamics and properties. As a first application of this method, we predict fast transfer of signals over long distances in polariton waveguides. Using the bistable behavior of the polaritons signals are automatically maintained at a clear logic level. This can be extended to a system with many nodes where the signal could jump from node to node without losing intensity, therefore creating an analogue of saltatory conduction in biological neurons, on potentially large distances. It would also be interesting in future work to generalize the present technique to non-resonant excitations, where bistability has also been studied [79–81]. The parameters are here taken for GaAs materials since bistability has been repeatedly observed in this material. We have focused on the treatment of inorganic-based microcavities. For organic materials, the treatment of (Frenkel-type) excitons as few-level molecules is more appropriate and was considered in a planar geometry with an FDTD-based method in [78]. However, for our proposal of saltatory conduction, organic materials are less suited given their larger linewidths, which make it difficult to achieve bistability. It also is possible to use materials with a higher difference in their refractive index such as TiO_2-SiO_2 or organic based microcavities [34], to increase the speed in the channel up to 20% of the speed of light and reach room-temperature operation, respectively. But unfortunately bistability has yet to be observed in such structures.

ACKNOWLEDGMENTS

K. D. and T. C. H. L. were supported by the Singapore Ministry of Education (MOE-T2EP50121-0020) and National Research Foundation project N-GAP (NRF2023-ITC004-001). H.S. acknowledges the Icelandic Research Fund (Rannis), Grant No. 217631-051 and 239552-051. P.M.W acknowledges grant EP/V026496/1 of EPSRC of the UK. The authors have no conflicts to disclose. The data that support the findings of this study are available from the corresponding author upon reasonable request.

Appendix A: On the differences between non-linear polariton description using Bloch equations and Kerr-type non linearity.

Existing FDTD algorithms allow for the description of linear excitons using linear response theory [52] or for the description of non linear crystals using Kerr-type terms [90]. However, neither of these algorithms or even a version combining the two mechanisms is adapted to describe exciton-polaritons in the non-linear regime. In this section we will stress the fundamental differences between our approach and

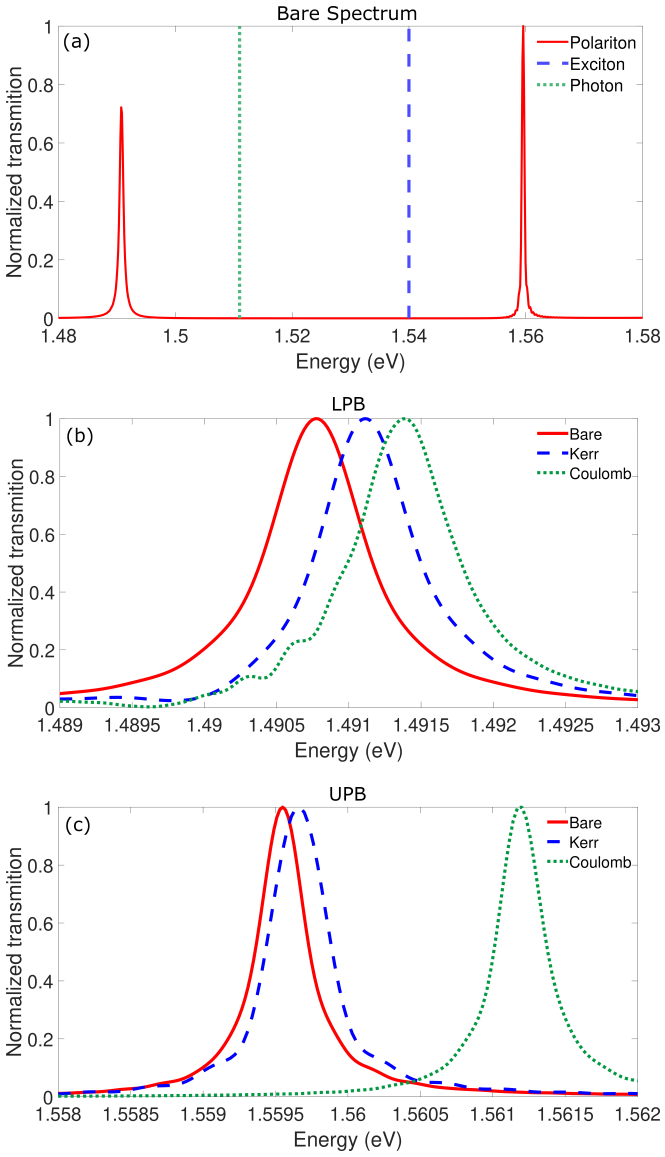

Figure 5: (a) Polariton spectrum (red line) in the linear regime for a 0D microcavity calculated using the FDTD algorithm. The dashed blue (green) corresponds to the exciton (photon) resonance. (b-c) Blueshifted (Lower-Upper) polariton resonance considering Kerr-type (blue dashed) or Coulomb-type (green dot dashed) nonlinearity close to the lower/upper polariton resonance.

a Kerr-type non-linear system combined with linear response theory.

Blueshift in non-linear polariton systems is responsible for many effects as it drastically changes the properties of the system. Its accurate description is therefore necessary to be able to describe, design and optimize any kind of advanced polariton system. We therefore performed a comparison on how a simple 1D system blueshifts depending on which approach is used. Predictably, the Kerr-type non-linearity induces a blueshift of the photon mode and does not change the exciton resonance whereas the Coulomb-type non-linearity blueshifts the exciton mode and does not change the photon mode. Therefore, the blueshift dependent polariton Hopfield coefficients, that describe the exciton and photon fractions, the dissipation rate, the interaction strength and the effective mass, change differently whether the blueshift is due to Kerr-type or Coulomb-type non-linearity. Moreover, it is commonly understood that "In the case of negative cavity detuning, the lower polariton is photon-like, while the upper polariton is exciton-like. Since the polariton interaction originates from the excitonic part of the polariton, the blueshift is larger for the upper polariton than for the lower one." [91]. We therefore considered a negative detuning cavity and compared the blueshifts of the upper and lower branches for both approaches. The results are shown in Figure 5. We observe that in the Kerr-type non-linearity case, the branches blueshift in the opposite behaviour to what is observed in polariton systems, while our model using Coulomb-type non-linearity is in agreement with this fundamental behaviour.

Also, an accurate description of the polariton at finite k is crucial. Indeed, effects such as polariton optical parametric oscillation and polariton optical parametric amplification require a completely accurate description of the frequency and intensity dependent photonic and excitonic fractions, effective masses, and losses of both polariton branches over the broadband spectral range corresponding to several times the Rabi splitting. Just one example of how Kerr nonlinearity fails to capture the correct physics is that the LPB converges at high k towards the bare exciton resonance, no matter what is the blueshift in the system. This is incorrect as when the LPB blueshifts, it should converge to a blueshifted exciton resonance. This effect can only be accurately described introducing the non-linearity in the excitonic component, as is done in our model.

Appendix B: Finite Difference Time Domain Method Formalism

The principle of the now famous FDTD is to evolve in the time domain the Maxwell equations with a non-uniform refractive index. In this part we will describe the formalism used to obtain the main results of this paper. We will here follow the description given by [82]. The novelty of our method lies partly in the way the exciton is introduced and in the inclusion of the non-linearity through the Bloch equations. We will first introduce the purely photonic evolution equations and compare the results with other methods as benchmarks. Second we will describe how the active exciton layer is considered and again compare the results to methods known to be correct. Finally the non-linear interaction between excitons will be added to the evolution equation.

Even though we here do not include the divergence equations into the formalism, they serve as a good test for the validity of the calculated fields. Indeed after solving for $\mathbf{H}$ and $\mathbf{E}$, using the constitutive relations, the fields $\mathbf{D}$ and $\mathbf{B}$ should satisfy the divergence equations. In the Cartesian coordinates, the Maxwell curl equations (6) can be written in the form of six equations, two for each dimension of space. The FDTD algorithm can be written in three-dimensions but since we have

translational symmetry in the z-direction, the set of equations can be simplified and expressed as:

$$\frac{\partial E_x}{\partial t} = \frac{1}{\varepsilon}\left(\frac{\partial H_z}{\partial y} - J_{bx} - \sigma_e^x E_x\right) \tag{B1a}$$
$$\frac{\partial E_y}{\partial t} = \frac{1}{\varepsilon}\left(-\frac{\partial H_z}{\partial x} - J_{by} - \sigma_e^y E_y\right) \tag{B1b}$$
$$\frac{\partial E_z}{\partial t} = \frac{1}{\varepsilon}\left(\frac{\partial H_y}{\partial x} - \frac{\partial H_x}{\partial y} - J_{bz} - \sigma_e^z E_z\right) \tag{B1c}$$
$$\frac{\partial H_x}{\partial t} = -\frac{1}{\mu_0}\left(\frac{\partial E_z}{\partial y} + \sigma_m^x H_x\right) \tag{B1d}$$
$$\frac{\partial H_y}{\partial t} = \frac{1}{\mu_0}\left(\frac{\partial E_z}{\partial x} - \sigma_m^y H_y\right) \tag{B1e}$$
$$\frac{\partial H_z}{\partial t} = \frac{1}{\mu_0}\left(\frac{\partial E_x}{\partial y} - \frac{\partial E_y}{\partial x} - \sigma_m^z H_z\right) \tag{B1f}$$

The FDTD method relies on the Yee algorithm [51] that updates the magnetic and electric fields at every point of space at every step of a time-marching iteration. Both fields and auxiliary fields need to be updating and therefore sampled at discrete positions and times. Since both fields are interdependent, they cannot be updated simultaneously nor measured at the same positions. Therefore we choose to update the magnetic field at times $(n+1/2)\Delta t$ and the electric one at time $n\Delta t$ where n in a positive integer and Δt is the time-sampling period. Moreover sampling points of the fields are chosen following a specific grid [51] allowing to treat the magnetic and electric fields separately. We choose to use a Cartesian grid since it fits to the geometry of our problem. We write (i,j,k) as the index of the point at the position (x,y,z). The fields are sampled following:

$$\begin{aligned}
&E_x(i,j,k) \to E_x((i-0.5)\Delta_x,(j-1)\Delta_y,(k-1)\Delta_z)\\
&E_y(i,j,k) \to E_y((i-1)\Delta_x,(j-0.5)\Delta_y,(k-1)\Delta_z)\\
&E_z(i,j,k) \to E_z((i-1)\Delta_x,(j-1)\Delta_y,(k-0.5)\Delta_z)\\
&H_x(i,j,k) \to H_x((i-1)\Delta_x,(j-0.5)\Delta_y,(k-0.5)\Delta_z)\\
&H_y(i,j,k) \to H_y((i-0.5)\Delta_x,(j-1)\Delta_y,(k-0.5)\Delta_z)\\
&H_z(i,j,k) \to H_z((i-0.5)\Delta_x,(j-0.5)\Delta_y,(k-1)\Delta_z)
\end{aligned} \tag{B2}$$

where Δ_x, Δ_y and Δ_z are the grid cell sizes respectively in the x, y and z directions. For simplicity we note the field sampled at the point (i,j,k) at the time $n\Delta_t$ as $\Psi^n(i,j,k)$ while keeping in mind the transformations above.

In order to update the value of the fields sampled on the Yee grid, we choose to write the derivatives using the first order accurate forward or backward finite differences method i.e.

$$\begin{aligned}
\frac{\partial \Psi^n(i,j,k)}{\partial t} &= \frac{\Psi^{n+1}(i,j,k)-\Psi^n(i,j,k)}{\Delta t}\\
\frac{\partial \Psi^n(i,j,k)}{\partial x} &= \frac{\Psi^n(i+1,j,k)-\Psi^n(i,j,k)}{\Delta x}\\
\frac{\partial \Psi^n(i,j,k)}{\partial y} &= \frac{\Psi^n(i,j,k)-\Psi^n(i,j-1,k)}{\Delta y}\\
\frac{\partial \Psi^n(i,j,k)}{\partial z} &= \frac{\Psi^n(i,j,k+1)-\Psi^n(i,j,k)}{\Delta z}.
\end{aligned} \tag{B3}$$

where Ψ represents any field on the Yee grid. The choice of the forward or backward case will depend on the position of the fields in the Yee grid. Combining equation B3 with the transformations in B2, the overall FDTD update equations will be based on the central finite difference scheme.
Similarly, since some field terms in the considered Maxwell equations may need to be sampled at undefined times and positions (i.e. $(n+1/2)\Delta t$ for the electric field), we consider the dependence between two cells to be linear:

$$\begin{aligned}
\Psi^{n+1/2}(i,j,k) &= \frac{\Psi^{n+1}(i,j,k)+\Psi^n(i,j,k)}{2}\\
\Psi^n(i,j,k) &= \frac{\Psi^{n+1/2}(i,j,k)+\Psi^{n-1/2}(i,j,k)}{2}.
\end{aligned} \tag{B4}$$

In order to verify the validity of this approximation, we run for each result a resolution convergence test i.e. we verify that the obtained result does not change with reduction of the size of the cell.

Applying these methods to (B1a), (B1b) and (B1f), we get the following evolution equations, linking the sampling-time $n\Delta t$ to the $(n+1)\Delta t$ one, for the six considered fields:

$$\begin{aligned}
E_\alpha^{n+1}(i,j,k) &= C_{e\alpha e}(i,j,k)E_\alpha^n(i,j,k) + C_{e\alpha J}(i,j,k)J_{b\alpha}^{n+1/2}(i,j,k)\\
&\quad + C_{e\alpha h\beta}(i,j,k)\left(H_\beta^{n+1/2}(i,j,k) - H_\beta^{n+1/2}(i-\delta_{\gamma x}, j-\delta_{\gamma y}, k-\delta_{\gamma y})\right)\\
&\quad + C_{e\alpha h\gamma}(i,j,k)\left(H_\gamma^{n+1/2}(i,j,k) - H_\gamma^{n+1/2}(i-\delta_{\beta x}, j-\delta_{\beta y}, k-\delta_{\beta z})\right)\\
H_\alpha^{n+1/2}(i,j,k) &= C_{h\alpha h}(i,j,k)H_\alpha^{n-1/2}(i,j,k)\\
&\quad + C_{h\alpha e\beta}(i,j,k)\left(E_\beta^n(i+\delta_{\gamma x}, j+\delta_{\gamma x}, k+\delta_{\gamma x}) - E_\beta^n(i,j,k)\right)\\
&\quad + C_{h\alpha e\gamma}(i,j,k)\left(E_\gamma^n(i+\delta_{\beta x}, j+\delta_{\beta x}, k+\delta_{\beta x}) - E_\gamma^n(i,j,k)\right).
\end{aligned} \tag{B5}$$

where (α,β,γ) is (x,y,z) in any cyclic permutation of the standard basis order.

It should be noted that these equations depend only on field sampled at the defined sample cells of the Yee grid. In order to obtain this result, we used the finite difference method along with the approximation of linear fields for small distances. The associated coefficients can be expressed as:

$$
\begin{aligned}
C_{e\alpha e}(i,j,k) &= \frac{2\varepsilon(i,j,k)-\Delta t\,\sigma_e^{\alpha}(i,j,k)}{2\varepsilon(i,j,k)+\Delta t\,\sigma_e^{\alpha}(i,j,k)}\\
C_{e\alpha J}(i,j,k) &= -\frac{2\Delta t}{2\varepsilon(i,j,k)+\Delta t\,\sigma_e^{\alpha}(i,j,k)},\\
C_{e\alpha h\beta}(i,j,k) &= -\frac{2\Delta t}{(2\varepsilon(i,j,k)+\Delta t\,\sigma_e^{\alpha}(i,j,k))\,\Delta\gamma},\\
C_{e\alpha h\gamma}(i,j,k) &= \frac{2\Delta t}{(2\varepsilon(i,j,k)+\Delta t\,\sigma_e^{\alpha}(i,j,k))\,\Delta\beta},\\
C_{h\alpha h}(i,j,k) &= \frac{2\mu_0-\Delta t\,\sigma_m^{\alpha}(i,j,k)}{2\mu_0+\Delta t\,\sigma_m^{\alpha}(i,j,k)},\\
C_{h\alpha e\beta}(i,j,k) &= -\frac{2\Delta t}{(2\mu_0+\Delta t\,\sigma_m^{\alpha}(i,j,k))\,\Delta\gamma},\\
C_{h\alpha e\gamma}(i,j,k) &= \frac{2\Delta t}{(2\mu_0+\Delta t\,\sigma_m^{\alpha}(i,j,k))\,\Delta\beta}.
\end{aligned}
\tag{B6}
$$

Once all these coefficients are defined, we start a time loop that allows to evolve the system starting from defined initial conditions (usually fields set to zero on the Yee grid).During each iteration n of a marching time loop, the magnetic field components are first updated for the time step $(n+0.5)$ according to the second set of equations in (A5). Following this, the electric field components are updated for the time step $(n+1)$ using the first set of equations in A5 [82].

The geometry of the considered system is encoded in these coefficients that are fixed before the marching time loop is started. Choosing carefully the spatial distribution of the permittivity we can therefore simulate the evolution of arbitrary geometries. The main issue with this formalism is that it does not yet include exciton resonances, light-matter coupling and exciton-exciton interaction. In order to solve this issue we need to introduce the exciton as an auxiliary field. We consider the same approximations under which Eqs (26) and (27) of Ref [54] were derived and re-express the polarization and exciton population Bloch equations as:

$$
i\frac{\partial \mathbf{P}}{\partial t} = (\omega_0 - i\gamma)\,\mathbf{P} - \Omega\mathbf{E} + \alpha N\mathbf{P} \tag{B7}
$$

$$
\frac{\partial N}{\partial t} = -2\,\mathrm{Im}\,(\Omega\mathbf{E}\cdot\mathbf{P}^{*}) \tag{B8}
$$

where we have neglected the renormalization of the exciton kinetic energy and the saturation of the Rabi splitting. The polarization vector can be related to the bound charge current through:

$$
\mathbf{J_b} = \frac{\partial \mathbf{P}}{\partial t}. \tag{B9}
$$

Sampling on the Yee Grid, using the FDTD method and cell to cell linear behaviour approximation we can write the update equations for the polarization and the exciton population:

$$
\begin{aligned}
\mathbf{J_b}^{n+1/2}(i,j) &= -\mathbf{J_b}^{n-1/2}(i,j) + C_{jp}\mathbf{P^n}(i,j) + C_{je}\mathbf{E^n}(i,j) + C_{jpn}N^{n-1/2}(i,j)\mathbf{P^n}(i,j)\\
&\quad + C_{jepp}\,\mathrm{Im}\,(\mathbf{E}^{n}(i,j)\cdot\mathbf{P}^{n*}(i,j))\,\mathbf{P}^{n}(i,j)\\
N^{n+1/2}(i,j) &= C_{nep}\,\mathrm{Im}\,(\mathbf{E}^{n}(i,j)\cdot\mathbf{P}^{n*}(i,j)) + N^{n-1/2}(i,j),
\end{aligned}
\tag{B10}
$$

where the coefficients are:

$$
\begin{aligned}
&C_{jp} = -2\,(\gamma + i\omega_0);\; C_{je} = 2i\Omega\\
&C_{jpn} = -2i\alpha;\; C_{jepp} = -i\alpha\Omega\Delta t;\; C_{nep} = -2\Omega\Delta t
\end{aligned}
\tag{B11}
$$

The current J_b is to be updated only at the location of the quantum wells or active layers. The rest of the grid is updated using the optical update equation (B5).

Now that we defined the evolution equations for the system, we need to introduce sources. Since we want to study the dynamics of the system when submitted to time-dependent incident fields, we choose to use a soft far source, i.e., several wavelengths away from the system, soft meaning that the source does not act like a defect on the grid. The source waveform needs to be chosen carefully such that the range of energies studied is adapted to the task since the waveform in the time-domain will define the waveform in the frequency domain. First we write the update equation at the position of the source for the magnetic field:

$$
H_z^{n+1/2}(i_S,j_S) = H_z^{n-1/2}(i_S,j_S) \tag{B12}
$$

$$
\quad + C_{hzm}(i_S,j_S) f_S(i_S,j_S,t) \tag{B13}
$$

where (i_S, j_S) are the sampling points where the source is non-zero and :

$$C_{hzm} = \frac{-2\Delta t}{2\mu_0 + \Delta t \sigma_m^z(i_S, j_S)}. \tag{B14}$$

The source is here introduced in the evolution equations as a magnetic current density. f_S corresponds here to the distribution of the source in space and time. Depending on the task the algorithm is performing, it can take various forms.

Appendix C: Bragg Mirrors, Planar Cavity and Polariton reflectivity spectrums

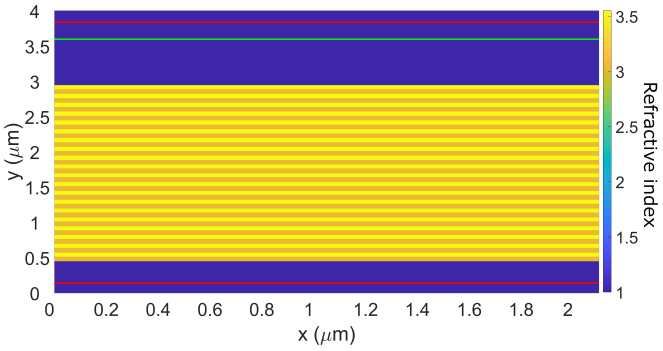

Figure 6: Distribution of the refractive index on the Yee-Grid for the FDTD simulation of the Bragg mirror reflectivity spectrum. The green line represents the position of the far field source, the red lines the edge of the PMLs. The field is measured just below the top PML line.

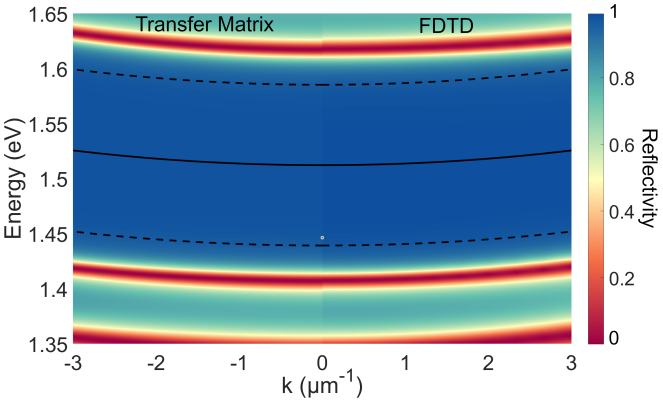

Figure 7: Comparaison of the TMM (left side) and FDTD (right side) results for a Bragg mirror consisting of 20 pairs of $Ga_{05}Al_{95}As/Ga_{20}Al_{80}As$. The results are in good agreement, the error is low close to $k = 0$ but increase as the light cone gets close. The dotted (full) black lines correspond to the edges (center) of the stop band obtained analytically. The colorscale represents the reflectivity.

In order to study the properties of the considered system and the response of our system to diverse kinds of excitation,

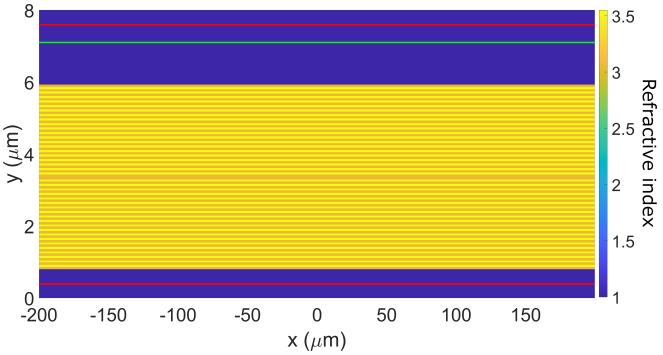

Figure 8: Distribution of the refractive index on the Yee-Grid for the FDTD simulation of the microcavity reflectivity spectrum. The green line represents the position of the far field source, the red lines the edge of the PMLs. The field is measured just below the top PML line.

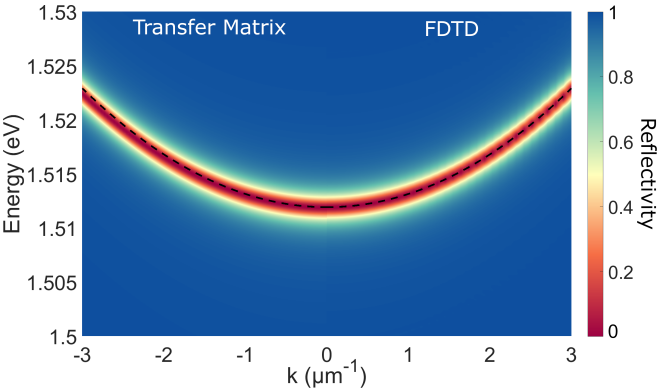

Figure 9: Planar cavity dispersion, calculated using TMM (left) and FDTD (right). The dashed line correspond to the theoretical dispersion. The colorscale represents the reflectivity.

we need to be able to calculate the dispersion of our exciton-polariton system. We will here work with well studied systems: the Bragg mirror and planar microcavity. In order to obtain a complete dispersion for a wide range of energies and k-vectors, there are two main options. The first option is based on the constant horizontal wavenumber method where one injects a planewave pulse for each k-vector and measures the transmission associated with it. Since each simulation run involves a unique k-vector, Bloch's theorem can be invoked, allowing calculations to be made with only one unit cell. The second option would be an injection with a dipole pulsed source, exciting all k-vectors simultaneously. Fourier transforming in space and time on the transmission plane gives us the dispersion of the system. However, for a clear resolution of the dispersion in k-space, one needs to model multiple unit cells with a significantly larger number of points as compared to the first option. Although the first option requires multiple iterations, they can be parallelised. Thus, we have opted to use the first option.

The source we consider is a 0.1 fs long Gaussian pulse,

centered in energy close to center of the stop band. In order for most of the pulse to be injected in the system we delay the pulse by 0.5 fs from the beginning of the simulation. The position of the source is chosen such that all structures are at least 20 wavelengths away. We can then express the source as:

$$f_S(t,x) = \exp\left(-\frac{(t-5\tau)^2}{\tau^2}\right)\exp\left(i\frac{E_0 t}{\hbar}\right)\exp(ik_x x) \quad \text{(C1)}$$

where E_0 is the center energy of the pulse and τ is the temporal width and k_x is the longitudinal wavevector of the emitted plane wave.

Now that we defined the sources, we need to define boundary conditions for our system such that the fields can decay without being reflected. The most efficient way to do so is to use the so-called Perfect Matched Layer method (PML). The PML method consists in creating a thick layer, at some or all edges of the system, in which the field decays. The non-reflective property of the PML must exist at all frequencies since the incoming field is broadband, which excludes the use of any isotropic classical material. This issue can be solved by using a virtual material such that its electric and magnetic conductivites are anisotropic. The different conductivities are then chosen such that the reflectivity of the layer is zero at all frequencies [84]. The PML conductivities, considering polynomial decay, can be expressed as [82] :

$$\begin{aligned}\sigma_{max} &= \frac{-3\varepsilon_0 c\ln\left(10^{-8}\right)}{2L_{PML}}\\ \sigma_e^y(i,j) &= \sigma_{max}\left(\frac{r(i,j)}{L_{PML}}\right)^2\\ \sigma_m^z(i,j) &= \sigma_e^y(i,j)\frac{\mu_0}{\varepsilon_0}\end{aligned} \quad \text{(C2)}$$

where L_{PML} is the thickness of the PML layer, r is the distance between the edge of the PML and the sampled point (i,j).

In order to confirm the validity of our approach we will now calculate the reflectivity of different structures and compare to the results of a method that has shown excellent agreements with experiments, namely the transfer-matrix methods (TMM) [83, 85, 86]. The first system we consider is a $Ga_{0.05}Al_{0.95}As(1)/Ga_{0.80}Al_{0.2}As(2)$ Bragg-Mirror. We consider the refractive indices to be $n_1 = 3.05$ and $n_2 = 3.55$ [87]. In the case of the FDTD we make the approximation that the refractive index is constant for the range of energies we consider. This approximation is not applied for the case of the TMM. The center of the stop band is chosen to be close to the GaAs exciton resonance i.e. $E_{sb} = 1.512$eV or $\lambda_{sb} = 820$ nm. The Bragg interference condition reads [83]:

$$n_1 L_1 = n_2 L_2 = \frac{\lambda_{csb}}{4}, \quad \text{(C3)}$$

where λ_{csb} is the wavelength of the center of the stop band. Therefore the thicknesses of the layers are $L_1 = 67.2$nm and $L_2 = 57.7$ nm. The mirror consists of 20 pairs of layers. In order to confirm the validity of our approaches, we also compare the calculated center and edges of the stop bands with the theoretical ones that can be expressed, in the case of TE polarization, as [83, 88, 89]:

$$E_{csb} = \frac{\hbar\pi c}{2(a+b)}\frac{n_a\cos(\phi_A)+n_b\cos(\phi_b))}{n_a n_b\cos(\phi_A)\cos(\phi_B)} \quad \text{(C4)}$$

$$E_{esb} = E_{csb}\left(1\pm\frac{2}{\pi}\sin^{-1}\left(\frac{n2-n1}{n2+n1}\right)\right) \quad \text{(C5)}$$

where E_{csb} and E_{esb} are respectively the energies at the center and edges of the stop band. ϕ_i are the propagation angles in the layer i of the mirror and can be linked to the angle of incidence ϕ_0 on the system by Snell's law : $n_i\sin(\phi_i) = \sin(\phi_0)$. The dispersions calculated by the TMM and by the FDTD are shown side by side in Figure 7 along with the analytical center and edges of the stop band. The left panel shows the reflectivity of the single Bragg mirror calculated by the TMM, the right panel the reflectivity calculated using the FDTD algorithm. Both the TMM and FDTD calculations are in excellent agreement with the analytical expression and with each other. Since the edges of the stop band represent when the Bloch wavenumber goes from imaginary to real, it is located at an energy where the reflectivity is very high, and therefore only seems to be inside the stop band.

We now calculate the dispersion of a $\lambda/2$ cavity built using the same Bragg mirror we studied. Similarly to the single Bragg mirror calculations, we compare the results given by the TMM and the FDTD to the theoretical dispersion (see Figure 9). As for the single bragg mirror, we obtained an excellent agreement between the different methods. The theoretical dispersion of the cavity mode is calculated in TE using [83, 89] :

$$\hbar\omega = \frac{L_c\omega_c(\theta)+L_{DBR}(\theta)\omega_S(\theta)}{L_c+L_{DBR}(\theta)}, \quad \text{(C6)}$$

where L_c is the thickness of the cavity and

$$\omega_s(\theta) = \frac{\pi c}{2(a+b)}\frac{n_a\cos(\theta_a)+n_b\cos(\theta_b)}{n_a n_b\cos(\theta_a)\cos(\theta_b)} \quad \text{(C7)}$$

$$L_{DBR} = \frac{2n_a^2 n_b^2(a+b)\cos(\theta_a)^2\cos(\theta_b)^2}{n_c^2\left(n_a^2-n_b^2\right)} \quad \text{(C8)}$$

$$\omega_c = \frac{\pi c}{n_c L_c\cos(\theta_c)} \quad \text{(C9)}$$

In order to compare directly our FDTD algorithm to experimental results, we simulated the structure presented in [72]. The structure simulated is displayed on Figure 10. We here consider two Bragg mirrors made of respectively 23 and 27 pairs of $GaAs/Ga_{0.15}Al_{0.85}As$ layers with thicknesses $L_{GaAlAs} = 68.2nm$, $L_{GaAs} = 57.6nm$ and refractive indices $n_{GaAlAs} = 3.096$, $n_{GaAs} = 3.666$. The microcavity between the two mirrors is composed by layers in order: a 89.4 nm thick GaAs layer, two 10 nm thick GaAs QWs surrounded

and separated by 10 nm thick $In_{0.04}Ga_{0.96}As$ layers with refractive index $n_{In_{0.04}Ga_{0.96}As} = 3.756$ and finally a 89.4 nm thick GaAs layer. We calculated the transmission of the structure using the same method as previously but measuring in transmission below the structure instead. The comparison between the simulation result and the experimental data is displayed in Figure 11. The excellent agreement shows that our method is suitable for simulating real devices.

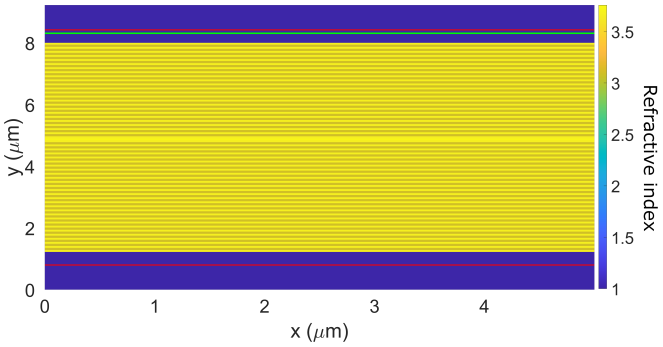

Figure 10: Distribution of the refractive index on the Yee-Grid for the FDTD simulation of the microcavity structure from [72].

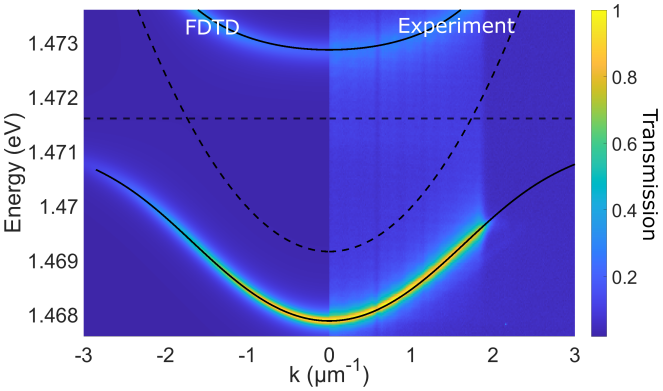

Figure 11: Planar cavity dispersion, calculated using FDTD (left) and measured experimentally (data from [72]). The colorscale represents the transmission. The dashed lines represent the photon and exciton modes, the full lines represent the upper and lower polariton branches calculated using coupled oscillator model.

Appendix D: Comparaison to other microstuctures

As mentionned in the main text, one of the advantages of the NL-FDTD for polaritons is the possibility to optimize a structure with respect to one or several figures of merit. In order to understand how figures of merits, chosen here as the signal velocity and the transferred intensity, depend on various parameters we simulated our structure varying the channel length and its refractive index.

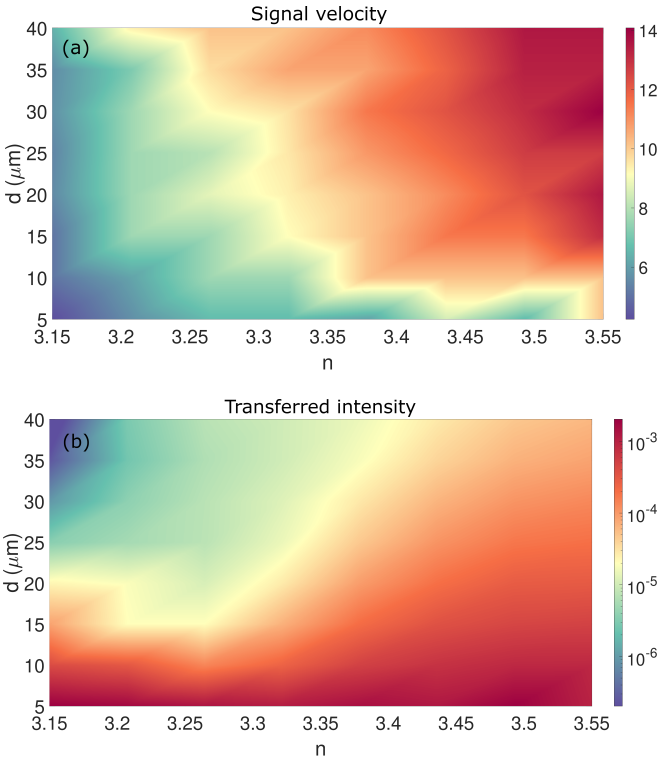

Figure 12: (a) Phase diagrams of the signal velocity in μm.ps^{-1} and (b) of the transferred intensity (normalized to the injected intensity) from node to node with respect to the distance between the nodes and the refractive index of the channel.

In order to measure the signal velocity, we excited at $t = 2.6ps$ the left node with a $1ps$ long pulse slightly blue detuned from the LPB with a power equivalent to 10% of the bistability threshold. We run the simulation for 10ps for each set of parameters. The velocity is obtained by calculating the time delay between the peak in the first node and the one in the second and dividing by the distance between the two nodes. The transferred intensity corresponds to the temporally and spatially integrated intensity in the second node divided by the one in the first one. It should be noted that the small intensity directly injected by the pump into the second node is removed in the calculation of this ratio. We obtain the two phase diagrams displayed in Figure 12. One can observe that as it can be expected, the transferred intensity decreases quickly with the distance between the nodes. Also, for large distances there is a clear advantage in using higher refractive indices as the transferred intensity is two orders of magnitude stronger for refractive index of 3.55 than for 3.15.

[1] I. Carusotto, and C. Ciuti, "Quantum fluids of light", Reviews of Modern Physics **85** 299-366 (2013).

[2] F. Manni, K. G. Lagoudakis, T. K. Paraiso, R. Cerna, Y. Leger, T. C. H. Liew, I. A. Shelykh, A. V. Kavokin, F. Morier-Genoud, and B. Deveaud-Pledran, "Spin-to-orbital angular momentum conversion in semiconductor microcavities", Phys. Rev. **B** 83, 241307(R) (2011).

[3] J.K. Chana, M. Sich, F. Fras, A.V. Gorbach, D.V. Skryabin, E. Cancellieri, E.A. Cerda-Mendez, K. Biermann, R. Hey, P.V. Santos, M.S. Skolnick, and D.N. Krizhanovskii, "Spatial Patterns of Dissipative Polariton Solitons in Semiconductor Microcavities", Phys. Rev. Lett. **115**, 256401 (2015).

[4] C. Leyder, T. C. H. Liew, A. V. Kavokin, I. A. Shelykh, M. Romanelli, J. Ph. Karr, E. Giacobino and A. Bramati, "Interference of Coherent Polariton Beams in Microcavities: Polarization-Controlled Optical Gates ", Phys. Rev. Lett. **99**, 196402 (2007).

[5] C. Adrados, A. Amo, T. C. H. Liew, R. Hivet, R. Houdre, E. Giacobino, A. V. Kavokin, and A. Bramati, "Spin Rings in Bistable Planar Semiconductor Microcavities ", Phys. Rev. Lett. **105**, 216403 (2010).

[6] C. Adrados, T. C. H. Liew, A. Amo, M. D. Martin, D. Sanvitto, C. Anton, E. Giacobino, A. Kavokin, A. Bramati, and L. Vina, "Motion of Spin Polariton Bullets in Semiconductor Microcavities", Phys. Rev. Lett. **107**, 146402 (2011).

[7] E. Wertz, A. Amo, D. D. Solnyshkov, L. Ferrier, T. C. H. Liew, D. Sanvitto, P. Senellart, I. Sagnes, A. Lemaitre, A. V. Kavokin, G. Malpuech, and J. Bloch, "Propagation and Amplification Dynamics of 1D Polariton Condensates", Phys. Rev. Lett. **109**, 216404 (2012).

[8] T. Gao, P. S. Eldridge, T. C. H. Liew, S. I. Tsintzos, G. Stavrinidis, G. Deligeorgis, Z. Hatzopoulos, and P. G. Savvidis,"Polariton condensate transistor switch", Phys. Rev. B **85**, 235102 (2012).

[9] S. R. K. Rodriguez, A. Amo, I. Sagnes, L. Le Gratiet, E. Galopin, A. Lemaître and J. Bloch, "Interaction-induced hopping phase in driven-dissipative coupled photonic microcavities", Nature Communications **7**, 11887 (2016).

[10] P. M. Walker, L. Tinkler, D. V. Skryabin, A. Yulin, B. Royall, I. Farrer, D. A. Ritchie, M. S. Skolnick and D. N. Krizhanovskii, "Ultra-low-power hybrid light–matter solitons", Nature Communications **6**, 8317 (2015).

[11] D. Liran, R. Rapaport, J. Hu, N. Lydick, H. Deng, and L. Pfeiffer, "Electrically Controlled Photonic Circuits of Field-Induced Dipolaritons with Huge Nonlinearities", Phys. Rev. X **14**, 031022 (2024).

[12] M. Kedziora, A. Opala, R. Mastria et al., "Predesigned perovskite crystal waveguides for room-temperature exciton–polariton condensation and edge lasing", Nat. Mater. (2024).

[13] P.M. Walker, L. Tinkler, B. Royall, D.V. Skryabin, I. Farrer, D.A. Ritchie, M.S. Skolnick, and D.N. Krizhanovskii, "Dark Solitons in High Velocity Waveguide Polariton Fluids", Phys. Rev. Lett. **119**, 097403 (2017).

[14] D. G. Suarez-Forero, F. Riminucci, V. Ardizzone, M. De Giorgi, L. Dominici, F. Todisco, G. Lerario, L. N. Pfeiffer, G. Gigli, D. Ballarini, and D. Sanvitto, "Electrically controlled waveguide polariton laser", Optica **7**, Issue 11, pp. 1579-1586 (2020).

[15] Zhaorong Wang, Bo Zhang, and Hui Deng, "Dispersion Engineering for Vertical Microcavities Using Subwavelength Gratings", Phys. Rev. Lett. **114**, 073601 (2015).

[16] V. Ardizzone, F. Riminucci, S. Zanotti, A. Gianfrate, M. Efthymiou-Tsironi, D. G. Suàrez-Forero, F. Todisco, M. De Giorgi, D. Trypogeorgos, G. Gigli, K. Baldwin, L. Pfeiffer, D. Ballarini, H. S. Nguyen, D. Gerace and D. Sanvitto, "Polariton Bose–Einstein condensate from a bound state in the continuum", Nature **605**,(2022).

[17] Jiaqi Hu, Nathanial Lydick, Zhaorong Wang, F. Jabeen, C. Schneider, S. Höfling, Hui Deng; Grating-based microcavity with independent control of resonance energy and linewidth for non-Hermitian polariton system. Appl. Phys. Lett. 22 August 2022; 121 (8): 081106.

[18] K. Winkler, O. A. Egorov, I. G. Savenko, X. Ma, E. Estrecho, T. Gao, S. Muller, M. Kamp, T. C. H. Liew, E. A. Ostrovskaya, S. Hofling, and C. Schneider, "Collective state transitions of exciton-polaritons loaded into a periodic potential", Phys. Rev. B **93**, 121303(R) (2016).

[19] S. Klembt, T. H. Harder, O. A. Egorov, K. Winkler, R. Ge, M. A. Bandres, M. Emmerling, L. Worschech, T. C. H. Liew, M. Segev, C. Schneider and S. Höfling, "Exciton-polariton topological insulator", Nature **562** (2018).

[20] G. Dasbach, C. Diederichs, J. Tignon, C. Ciuti, Ph. Roussignol, C. Delalande, M. Bayer, and A. Forchel, "Polarization inversion via parametric scattering in quasi-one-dimensional microcavities", Phys. Rev. B **71**, 161308(R) (2005)

[21] M. Klaas, O. A. Egorov, T. C. H. Liew, A. Nalitov, V. Markovic, H. Suchomel, T. H. Harder, S. Betzold, E. A. Ostrovskaya, A. Kavokin, S. Klembt, S. Hofling, and C. Schneider, "Nonresonant spin selection methods and polarization control in exciton-polariton condensates", Phys. Rev. B **99**, 115303 (2019).

[22] I. Gnusov, H. Sigurdsson, J.D. Topfer, S. Baryshev, S. Alyatkin, and P.G. Lagoudakis, "All-Optical Linear-Polarization Engineering in Single and Coupled Exciton-Polariton Condensates", Phys. Rev. Applied **16**, 034014 (2021).

[23] Yi-Cheng Liu and Tim Byrnes, "FDTD and transfer matrix methods for evaluating the performance of photonic crystal based microcavities for exciton-polaritons", Semicond. Sci. Technol. **31**, 115019 (2016).

[24] L. M. S. De Silva, and K. A. I. L. Wijewardena Gamalath, "Modelling of Exciton-Polaritons". World Scientific News, **106**, 194–213 (2018).

[25] A. Baas, J. Ph. Karr, H. Eleuch, and E. Giacobino, "Optical bistability in semiconductor microcavities", Phys. Rev. A **69**, 023809 (2004).

[26] M. De Giorgi, D. Ballarini, E. Cancellieri, F. M. Marchetti, M. H. Szymanska, C. Tejedor, R. Cingolani, E. Giacobino, A. Bramati, G. Gigli, and D. Sanvitto, "Control and Ultrafast Dynamics of a Two-Fluid Polariton Switch", Phys. Rev. Lett. **109**, 266407 (2012).

[27] R. Cerna, Y. Léger, T.K. Paraïso, M. Wouters, F. Morier-Genoud, M.T. Portella-Oberli and B. Deveaud, "Ultrafast tristable spin memory of a coherent polariton gas", Nat. Commun. **4**, 2008 (2013).

[28] A. Dreismann, H. Ohadi, Y. del Valle-Inclan Redondo, R. Balili, Y. G. Rubo, S. I. Tsintzos, G. Deligeorgis, Z. Hatzopoulos, P. G. Savvidis and J. J. Baumberg, "A sub-femtojoule electrical spin-switch based on optically trapped polariton condensates" Nat. Mater. **15**, 1074 (2016).

[29] H. Suchomel, S. Brodbeck, T. C. H. Liew, M. Amthor, M. Klaas, S. Klembt, M. Kamp, S. Höfling and C. Schneider, "Prototype of a bistable polariton field-effect transistor switch", Sci. Rep. **7**, 5114 (2017).

[30] J. Feng et al., "All-optical switching based on interacting ex-

citon polaritons in self-assembled perovskite microwires", Sci. Adv. **7**, eabj6627(2021).

[31] J. Zhao, A. Fieramosca, R..Bao, et al., "Room temperature polariton spin switches based on Van der Waals superlattices", Nat. Commun. **15**, 7601 (2024).

[32] D.A. Sannikov, A.V. Baranikov, A.D. Putintsev, et al., "Room temperature, cascadable, all-optical polariton universal gates", Nat. Commun. **15**, 5362 (2024).

[33] D. Ballarini, M. De Giorgi, E. Cancellieri, R. Houdré, E. Giacobino, R. Cingolani, A. Bramati, G. Gigli and D. Sanvitto, "All-optical polariton transistor", Nature Communications **4**, 1778 (2013).

[34] A. V. Zasedatelev, A. V. Baranikov, D. Urbonas, F. Scafirimuto, U. Scherf, T. Stöferle, R. F. Mahrt and P. G. Lagoudakis, "A room-temperature organic polariton transistor", Nature Photonics **13**, 378 (2019).

[35] A. Amo, T. C. H. Liew, C. Adrados, R. Houdré, E. Giacobino, A. V. Kavokin and A. Bramati, "Exciton–polariton spin switches", Nature Photonics **4**, 361 (2010).

[36] Y. Sun, Y. Yoon, S. Khan, L. Ge, M. Steger, L. N. Pfeiffer, K. West, H. E. Türeci, D. W. Snoke, and K. A. Nelson, "Stable switching among high-order modes in polariton condensates", Phys. Rev. B **97**, 045303 (2018).

[37] R. Keynes, D. Aidley, and C. Huang, (2011). "Cable theory and saltatory conduction". In Nerve and Muscle (pp. 63-73). Cambridge: Cambridge University Press.

[38] Dario Ballarini, Antonio Gianfrate, Riccardo Panico, Andrzej Opala, Sanjib Ghosh, Lorenzo Dominici, Vincenzo Ardizzone, Milena De Giorgi, Giovanni Lerario, Giuseppe Gigli, Timothy C. H. Liew, Michal Matuszewski, and Daniele Sanvitto, "Polaritonic Neuromorphic Computing Outperforms Linear Classifiers", Nano Letters, **20**, 3506-3512 (2020).

[39] Rafał Mirek, Andrzej Opala, Paolo Comaron, Magdalena Furman, Mateusz Król, Krzysztof Tyszka, Bartłomiej Seredyński, Dario Ballarini, Daniele Sanvitto, Timothy C. H. Liew, Wojciech Pacuski, Jan Suffczyński, Jacek Szczytko, Michał Matuszewski, and Barbara Piętka, Nano Letters, **21**, 3715-3720 (2021).

[40] K. Tyszka, M. Furman, R. Mirek, M. Król, A. Opala, B. Seredyński, J. Suffczyński, W. Pacuski, M. Matuszewski, J. Szczytko, B. Piętka, "Leaky Integrate-and-Fire Mechanism in Exciton–Polariton Condensates for Photonic Spiking Neurons." Laser Photonics Rev, **17**, 2100660 (2022).

[41] A. Opala, R. Panico, V. Ardizzone, B. Pietka, J. Szczytko, D. Sanvitto, M. Matuszewski, and D. Ballarini, "Training a Neural Network with Exciton-Polariton Optical Nonlinearity", Phys. Rev. Applied **18**, 024028 (2022).

[42] Andrzej Opala and Michał Matuszewski, "Harnessing exciton-polaritons for digital computing, neuromorphic computing, and optimization [Invited]," Opt. Mater. Express **13**, 2674-2689 (2023)

[43] R. Mirek, A. Opala, M. Furman, M. Król, K. Tyszka, B. Seredyński, W. Pacuski, J. Suffczyński, J. Szczytko, M. Matuszewski, and B. Piętka, "Neural Networks Based on Ultrafast Time-Delayed Effects in Exciton Polaritons" Phys. Rev. Applied **17**, 054037 (2022).

[44] M. Matuszewski, A. Opala, R. Mirek, M. Furman, M. Król, K. Tyszka, T.C.H. Liew, D. Ballarini, D. Sanvitto, J. Szczytko, and B. Piętka, "Energy-Efficient Neural Network Inference with Microcavity Exciton Polaritons", Phys. Rev. Applied **16**, 024045 (2021).

[45] M. Matuszewski, A. Prystupiuk, and A. Opala, "Role of all-optical neural network", Phys. Rev. Applied **21**, 014028 (2024).

[46] E. Sedov, A. Kavokin, "Polariton lattices as binarized neuromorphic networks", arXiv:2401.07232 (2024).

[47] M. Ossiander, M.L. Meretska, S. Rourke, et al. "Metasurface-stabilized optical microcavities", Nat Commun **14**, 1114 (2023).

[48] N.W.E Seet, K. Dini and T.C.H. Liew, "Optimization of Purcell-enhanced microcavities with the cylindrical finite-difference time-domain algorithm", Physical Review A **109** (4), 043509.

[49] A.P. Ovvyan, MK. Li, H. Gehring, et al. "An electroluminescent and tunable cavity-enhanced carbon-nanotube-emitter in the telecom band", Nat Commun **14**, 3933 (2023).

[50] K. Voronin, A. S. Taradin, M. V. Gorkunov, and D. G. Baranov, ACS Photonics, "Single-Handedness Chiral Optical Cavities" , **9**, 8, 2652–2659 (2022).

[51] K. S. Yee, "Numerical solution of inital boundary value problems involving Maxwell's equations in isotropic media", IEEE Transactions on Antennas and Propagation, vol. 14, pp. 302–307, 1966.

[52] Yong Zeng, Ying Fu, Mats Bengtsson, Xiaoshuang Chen, Wei Lu, and Hans Ågren, "Finite-difference time-domain simulations of exciton-polariton resonances in quantum-dot arrays", Opt. Express **16**, 4507-4519 (2008).

[53] H. Haug and S. W. Koch, "Quantum Theory of the Optical and Electronic Properties of Semiconductors ", Chapter 10, World Scientific (2009).

[54] G. Rochat, C. Ciuti, V. Savona, C. Piermarocchi, A. Quattropani, and P. Schwendimann, "Excitonic Bloch equations for a two-dimensional system of interacting excitons", Phys. Rev. B **61**, 13856 (2000).

[55] A. Amo, S. Pigeon, C. Adrados, R. Houdre, E. Giacobino, C. Ciuti, A. Bramati, "Light engineering of the polariton landscape in semiconductor microcavities" Phys. Rev. B **82**, 081301(R) (2010).

[56] V. Timofeev and D. Sanvitto, "Exciton Polaritons in Microcavities", Springer Berlin, Heidelberg, (2012).

[57] I Rosenberg, et al., "Strongly interacting dipolar-polaritons", Sci. Adv., **4**, eaat8880 (2018).

[58] E. Estrecho, et al., "Direct measurement of polariton-polariton interaction strength in the Thomas-Fermi regime of exciton-polariton condensation", Phys. Rev. B, **100**, 035306 (2019).

[59] D. Xu, A. Mandal, J. M. Baxter, S. Cheng, I. Lee, H. Su, S. Liu, D. R. Reichman and M. Delor, "Ultrafast imaging of polariton propagation and interactions", Nat. Comm.**14**, 3881 (2023).

[60] S. Yu, K. W. Kim, M. A. Stroscio, G. J. Iafrate, J.-P. Sun and G. I. Haddad, "Transfer matrix method for interface optical-phonon modes in multiple-interface heterostructure systems", J. Appl. Phys. **82**, 3363–3367 (1997).

[61] N. A. Gippius, I. A. Shelykh, D. D. Solnyshkov, S. S. Gavrilov, Yuri G. Rubo, A. V. Kavokin, S. G. Tikhodeev, and G. Malpuech, "Polarization Multistability of Cavity Polaritons", Phys. Rev. Lett. **98**, 236401 (2007).

[62] T. K. Paraiso, M. Wouters, Y. Leger, F. Morier-Genoud and B. Deveaud-Plédran , "Multistability of a coherent spin ensemble in a semiconductor microcavity", Nature Materials **9**,655–660 (2010).

[63] Y.V. Kartashov, V. V. Konotop, and L. Torner, "Compactons and bistability in exciton-polariton condensates", Phys. Rev. B **86**, 205313 (2012).

[64] D. Sarkar, S. S. Gavrilov, M. Sich, J. H. Quilter, R. A. Bradley, N. A. Gippius, K. Guda, V. D. Kulakovskii, M. S. Skolnick, and D. N. Krizhanovskii, "Polarization Bistability and Resultant Spin Rings in Semiconductor Microcavities", Phys. Rev. Lett. **105**, 216402 (2010).

[65] Y. V. Kartashov and D. V. Skryabin, "Bistable Topological Insulator with Exciton-Polaritons", Phys. Rev. Lett. **119**, 253904

(2017).

[66] S.V. Koniakhin, O. Bleu, D.D. Stupin, S. Pigeon, A. Maitre, F. Claude, G. Lerario, Q. Glorieux, A. Bramati, D. Solnyshkov, and G. Malpuech, “Stationary Quantum Vortex Street in a Driven-Dissipative Quantum Fluid of Light”, Phys. Rev. Lett. **123**, 215301 (2019).

[67] G. Grosso, S. Trebaol, M. Wouters, F. Morier-Genoud, M. T. Portella-Oberli, and B. Deveaud, “Nonlinear relaxation and selective polychromatic lasing of confined polaritons”, Phys. Rev. B **90**, 045307 (2014).

[68] A. A. Demenev, D. D. Yaremkevich, A. V. Scherbakov, S. M. Kukhtaruk, S. S. Gavrilov, D. R. Yakovlev, V. D. Kulakovskii, and M. Bayer, “Ultrafast-induced switching of a bistable cavity-polariton system”, Phys. Rev. B **100**, 100301(R) (2019).

[69] T. Espinosa-Ortega and T. C. H. Liew, “Complete architecture of integrated photonic circuits based on and and not logic gates of exciton polaritons in semiconductor microcavities”, Phys. Rev. B **87**, 195305 (2013).

[70] O. Kyriienko, H. Sigurdsson, and T. C. H. Liew, "Probabilistic solving of *NP*-hard problems with bistable nonlinear optical networks", Phys. Rev. B **99**, 195301 (2019).

[71] R Banerjee and T C H Liew, “Artificial life in an exciton-polariton lattice”, New J. Phys. **22**, 103062 (2020)

[72] C.E. Whittaker et al., "Polariton Pattern Formation and Photon Statistics of the Associated Emission", Phys. Rev. X **7**, 031033 (2017).

[73] T. C. H. Liew, A. V. Kavokin, and I. A. Shelykh, “Optical Circuits Based on Polariton Neurons in Semiconductor Microcavities” Phys. Rev. Lett. **101**, 016402 (2008).

[74] H. Sigurdsson, I. A. Shelykh, and T. C. H. Liew, “Switching waves in multilevel incoherently driven polariton condensates”, Phys. Rev. B **92**, 195409 (2015).

[75] G. Lerario, A. Cannavale, D. Ballarini, L. Dominici, M. De Giorgi, M. Liscidini, D. Gerace, D. Sanvitto, and G. Gigli, “Room temperature Bloch surface wave polaritons”, Optics Letters **39**,7 2068 (2014).

[76] G. Lerario, D. Ballarini, A. Fieramosca, A. Cannavale, A. Genco, F. Mangione, S. Gambino, L. Dominici, M. De Giorgi, G. Gigli and D. Sanvitto, “High-speed flow of interacting organic polaritons", Light Sci. Appl. **6**, e16212 (2017).

[77] O. El Daïf et al., "Polariton quantum boxes in semiconductor microcavities", Appl. Phys. Lett. **88**, 6, 061105 (2006).

[78] Z. Zhou, H. Chen, M. Sukharev, J. E. Subotnik, and A. Nitzan, "Nature of polariton transport in a Fabry-Perot cavity", Phys. Rev. A **109**, 033717 (2024).

[79] D. V. Karpov, I. G. Savenko, H. Flayac, and N. N. Rosanov, ’Dissipative soliton protocols in semiconductor microcavities at finite temperatures’, Phys. Rev. B **92**, 075305 (2015).

[80] M. Klaas, H. Sigurdsson, T. C. H. Liew, S. Klembt, M. Amthor, F. Hartmann, L. Worschech, C. Schneider, and S. Höfling, "Electrical and optical switching in the bistable regime of an electrically injected polariton laser", Phys. Rev. B **96**, 041301(R) (2017).

[81] L. Pickup, K. Kalinin, A. Askitopoulos, Z. Hatzopoulos, P. G. Savvidis, N. G. Berloff, and P. G. Lagoudakis, "Optical Bistability under Nonresonant Excitation in Spinor Polariton Condensates", Phys. Rev. Lett. **120**, 225301 (2018).

[82] A. Elsherbeni and V. Demir , "The Finite-Difference Time-Domain Method for Electromagnetics with MATLAB Simulations (Electromagnetic Waves)", SciTech Publishing (2015).

[83] A. Kavokin, J. J. Baumberg, G. Malpuech, F. P. Laussy, Microcavities, Oxford University Press, Oxford, UK (2017).

[84] J. Berenger, “A perfectly matched layer for the absorption of electromagnetic waves,” J. Comput. Phys., vol. **114**, pp. 185–200, (1994).

[85] Vladimirova, M., Kavokin, A. and Kaliteevski, M. Dispersion of bulk exciton polaritons in a semiconductor microcavity. Phys. Rev. B **54**, 14566 (1996).

[86] Krisnanda, T. et al. Room Temperature Light-Mediated Long-Range Coupling of Excitons in Perovskites. Adv. Opt. Mater. **9**, 2001835 (2021).

[87] S. Adachi, "GaAs, AlAs, and AlxGa1-xAs: Material parameters for use in research and device applications", Journal of Applied Physics **58**, R1 (1985).

[88] B. Osting, "Bragg structure and the first spectral gap", Applied Mathematics Letters **25** 1926-1930 (2012).

[89] G. Panzarini, L. C. Andreani, A. Armitage, D. Baxter, M. S. Skolnick, V. N. Astratov, J. S. Roberts, A. V. Kavokin, M. R. Vladimirova and M. A. Kaliteevski, "Cavity-polariton dispersion and polarization splitting in single and coupled semiconductor microcavities", Physics of the Solid State volume **41**, 1223–1238 (1999).

[90] B. Salski, T. Karpisz, and R. Buczynski, "Electromagnetic Modeling of Third-Order Nonlinearities in Photonic Crystal Fibers Using a Vector Two-Dimensional FDTD Algorithm" J. Light. Technol., **33**, 13, 2905 (2015).

[91] B. Deveaud, "Polariton interactions in semiconductor microcavities", Comptes Rendus. Physique, **17** 8,874-892, (2016).